Effects of Plant and Scene Modeling on Canopy NDVI Simulation: A Case Study on Phragmites Australis and Spartina Alterniflora

Zhu Tao, Runhe Shi ⓘ, Jean-Philippe Gastellu-Etchegorry, Jiayin Shi, Nan Wu, Bo Tian, and Wei Gao

Abstract—**Plant and scene three-dimensional (3-D) modeling, combined with radiative transfer (RT) modeling, are of great importance for mastering canopy reflectance characteristics and further developing target recognition and parameter retrieval in remote sensing images. However, 3-D RT simulation of large, complex landscapes is generally too demanding in terms of computing time and memory space. Simplifying plant models can significantly reduce the computational load, but with the accuracy reducing in radiation simulations. It is necessary to balance the complexity of plant models and the efficiency of 3-D RT simulation while maintaining high simulation accuracy. We investigated this issue for the vegetation of the Yangtze River estuary in eastern China. First, we used a series of created 3-D models of two species (Phragmites australis and Spartina alterniflora) to simulate canopy reflectance with the discrete anisotropic radiative transfer (DART) model. Then, we investigated how the simulated plant model complexity, plant density, and scene unit scale influence the accuracy and computation time of canopy normalized difference vegetation index (NDVI) simulation. The comparison of different parameterization simulations leads to three major conclusions. It is not necessary to simulate the actual vegetation density exactly, given the simplifications and approximations inherent in simulations. A specific 3-D model per species is needed for simulation since plants' morphological structures different. Simplifying plant 3-D models and using a coarser DART scale of analysis shortens simulation time, but decreases the accuracy of the simulated canopy NDVI to varying degrees. Based on these results, we propose a universal optimization scheme that balances the accuracy and computation time of canopy NDVI simulation.**

Index Terms—**Discrete anisotropic radiative transfer (DART), normalized difference vegetation index (NDVI), P. australis, S. alterniflora, three-dimensional (3-D) model.**

I. INTRODUCTION

PLANT canopy reflectance spectroscopy is very useful for studying vegetation and ecosystems with remote sensing. However, plant species, morphology, and environment greatly complicate the interpretation of the measured signals. For example, the spectra of canopies that contain the same species usually differ due to differences in terms of vegetation canopy structure and pigment content in leaves. Solar radiation interaction with plant elements, via absorption and scattering mechanisms, depends on leaf dimensions, orientations, and optical properties. Factors as the plant growth period [1], the internal growth gap [2]–[4], the geometry of individual shoots, and their spatial arrangement in a canopy strongly affect radiation mechanisms, including multiple scattering processes, and consequently strongly affect the canopy spectral reflectance [5]–[7]. Radiation Transfer (RT) models are very well adapted tools to describe and study these mechanisms [8]. Wu [9] defined an updated bidirectional reflectance distribution function (BRDF) suitable for random rugged terrain considering rugged terrain effects under the existing reflectance framework, which is based on the mountainous RT theory with realistic DEM prior knowledge. Biophysical parameters can be quantitatively retrieved by establishing a canopy radiation and scattering model and inverting it [10]. This is the case for clumping index [11], [12], leaf area index [13], [14], normalized difference vegetation index (NDVI) [15], [16], and also surface albedo [17], [18].

Numerous forward canopy reflectance models were developed to quantitatively retrieve canopy biophysical parameters from remote sensing observations [9], [19]–[27]. Traditional one-dimensional (1-D) RT models are often not suitable for reliable estimation of radiation-related quantities due to the spatial heterogeneity of the structure and physical properties [28]. 3-D RT models are usually designed to consider the 3-D architecture of plant canopies when simulating their spectral radiance. Therefore, they have the potential to account for the spectrally dependent anisotropic behavior of vegetation

Zhu Tao, Runhe Shi, Jiayin Shi, and Nan Wu are with the Key Laboratory of Geographic Information Science (Ministry of Education), School of Geographic Sciences, Joint Laboratory for Environmental Remote Sensing and Data Assimilation, Institute of Eco-Chongming, ECNU, Shanghai 200241, China (e-mail: taozhu.work@foxmail.com; rhshi@geo.ecnu.edu.cn; 51193901054@stu.ecnu.cn; 52183901014@stu.ecnu.cn).

Jean-Philippe Gastellu-Etchegorry is with the Centre d'Etudes Spatiales de la Biosphére (CESBIO), Centre National de la Recherche Scientifique (CNRS), Centre National d'Etudes Spatiales (CNES), Institut de Recherche pour le Développement (IRD), Université Paul Sabatier (Toulouse III), 31400 Toulouse, France (e-mail: jean-philippe.gastellu@iut-tlse3.fr).

Bo Tian is with the State Key Laboratory of Estuarine and Coastal Research, ECNU, Shanghai 200026, China (e-mail: btian@sklec.ecnu.edu.cn).

Wei Gao is with the Department of Ecosystem Science and Sustainability, Colorado State University, Fort Collins, CO 80523 USA (e-mail: wei.gao@colostate.edu).

Digital Object Identifier 10.1109/JSTARS.2021.3088580

canopies [29] and have the potential to accurately simulate the bidirectional reflectance and temperature distribution of Earth's surfaces, which can greatly improve information retrieval from remotely sensed images. Here, we consider the discrete anisotropic radiative transfer (DART) model [30]. It is one of the most comprehensive and accurate 3-D RT models to describe the radiation scattering characteristics of vegetation canopy based on 3-D scenes with different components, architecture, and spatial distribution characteristics. It is being developed by the CESBIO Laboratory since 1992 and is provided free for research and education by the Paul Sabatier University (France).[1] It simulates the radiative budget and remote sensing observations (i.e., *in-situ*/airborne/satellite imaging spectrometers and LiDARs) of natural and urban landscapes, including topography and atmosphere above and within the landscape, in the visible, near-infrared, and thermal infrared spectral regions [30]–[32]. Here, we used the DART's standard mode, called DART-FT. This mode tracks radiation with an adaptation of the so-called discrete ordinate method that tracks radiation in a finite number of discrete directions. Any natural and urban landscape is simulated as a 3-D array of cells that contain facets, fluids, and/or turbid material (i.e., infinite number of infinitely small plane elements characterized by their orientation, area density, and orientation). Here, scene elements (i.e., plants) are simulated as 3-D plant objects made of facets. DART can simulate any remote sensing configuration (i.e., any atmosphere condition, forest and crop growth stage, terrain geomorphology, date, viewing direction, and spatial and spectral resolution). It computes vegetation canopy directional reflectance, as well as brightness temperature at the bottom (BOA) and top (TOA) of the atmosphere [32]–[35].

The DART simulated scenes can be finite or infinite with the repetition of a finite pattern [36]. Here, we consider scenes that contain plants that are simulated as a distribution of 3-D plant models. Indeed, the turbid representation is not well adapted to represent the specific architecture of small plants. Traditional 3-D tree modeling technologies are categorized as image-based, rule-based, sketch-based, and laser-scanning-based methods. The 3-D plant model generated by the rule-based modeling method is relatively stiff and simple and the shape is not easy to control, which requires more professional botanical knowledge and greatly limits the type and shape for a 3-D plant model construction [37]–[40]. Sketch-based modeling requires a high level of professional drawing skills for users involved in modeling [41]–[43]. The modeling based on laser scanning data needs to deal with a large number of 3-D point cloud data, the processing of which can be computer-intensive [44], [45] and is not well adapted to vegetation elements as small plants. Image-based modeling methods can more realistically characterize the shape of plants and can give a more specific detailed vegetation model with a strong sense of reality [46], [47]. It is often accepted that a plant vegetation cover can be simulated with coarse 3-D plant models provided that the spatial resolution of analysis is large enough. Actually, if the plant cover is homogenous with a single plant species, the architecture of the individual plant element is expected to influence the radiance of the vegetation canopy. On
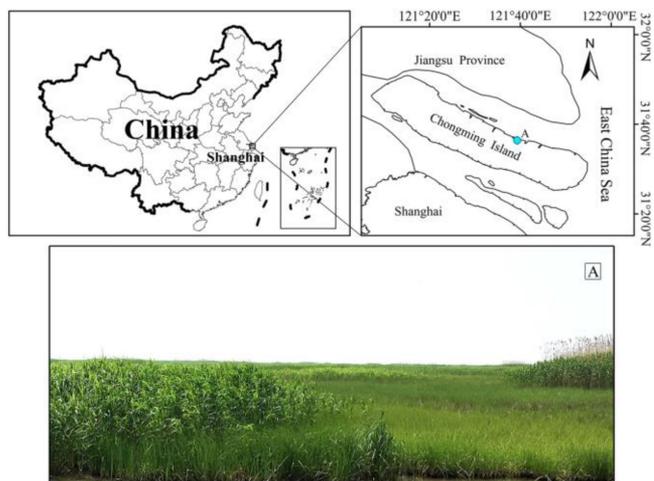

Fig. 1.   Location of the study area and display of *P. australis* and *S. alterniflora* plants.

the other hand, to simulate with a 3-D RT model, the radiance of a canopy where the architecture of plant elements is very accurately represented can require tremendous computer time and memory. How to render the real structures of vegetation effectively and efficiently is a prerequisite for studying the radiation regime [28]. In other words, a balanced strategy needs to be struck between the level of precision of 3-D plant models and the computer time and memory that are acceptable for 3-D models. From the perspective of 3-D modeling, the key to plant model simplification is to reduce the number of irregular triangular facets. However, the influence of this decrease on the accuracy of 3-D models should be known. How does the simplification of plant morphology influence the radiance of the canopy simulated by 3-D models? Moreover, this influence depends on the plant species if they have different architectures.

As an essential component of the terrestrial ecosystem, wetlands play a critical role in improving regional climate and ecological balance. In recent studies of wetlands, remote sensing technology has been widely used to monitor its biodiversity and dynamics changes. Here, we study the NDVI [48] of two important wetland species with large morphological differences, *P. australis* and *S. alterniflora*. NDVI is a commonly used index in remote sensing based studies of vegetation. Based on field-measured plant data on 1 m × 1 m quadrats (Fig. 1.), we created six 3-D plant models with different degrees of simplification for each species that we used to simulate the NDVI of vegetation canopies made of these plants. Section II shows the research area and data. Section III describes the process of 3-D object simplification using the tool "mesh smoothing" of 3ds Max,[2] the construction of 1 m × 1 m scenes with combinations of three kinds of parameters, and their DART simulated reflectance. Section IV analyzes the NDVI difference between the nadir and directional, and gradually selects suitable simulation scene projects. Then, proposes a widely adaptable criterion for selecting the optimum 3-D plant model, the best density, and cell dimensions when started a small-scale scene simulation in DART, and discusses current and future applications of the

---

[1]Online. [Available]: https://dart.omp.eu

[2]Online. [Available]: www.autodesk.com/products/3ds-max

TABLE I
MEAN PARAMETER VALUES OF *P. AUSTRALIS* AND *S. ALTERNIFLORA* PLANTS

Name	Height (cm)	Base stem width (cm)	Leaf number	Leaf length (cm)	Leaf width (cm)	Leaf spacing (cm)
P_average	221.9	0.77	10	28.0	1.4	9.2
S_average	156.2	0.76	8	29.9	1.0	6.3

work. Finally, a conclusion is given in Section V. In addition, examples of field-measured plant characteristics and simulation computation time are shown in Tables A1 to A4.

II. RESEARCH AREA AND DATA

A. Research Area

In-situ measurements for 3-D modeling were performed at the Dongtan Wetland Experiment Site on Chongming Island (Fig. 1.), in the well-developed Yangtze River estuary, Shanghai, China (31°25'–31°38'N, 121°50'–122°05'E). The measurements focused on the invasive species of *S. alterniflora* and the native species of *P. australis*, over an area of 32 600 ha. This area belongs to the northern subtropical marine climate with an annual mean temperature of 15.3 °C. Its rain spell mainly occurs in summer associated with the Meiyu front with annual mean precipitation of 1004 mm and relative humidity of 82% [49].

B. Measured Data

Growth parameters (plant height, leaf number, leaf length, leaf width, leaf spacing, base rhizome width, etc.) were measured for every sampled single plant (i.e., *S. alterniflora* and *P. australis*) in July and August for several months since this was the period when these plants reach their luxurious and vigorous stage. Based on their mean value (Table I), we created a series of 3-D plant models with different degrees of simplification per species.

III. PLANT MODELING AND SCENE MODELING

A. Individual Plant Modeling

In most cases, plants consist of a large number of individual elements, the configuration of which follows relatively simple rules (e.g., constant branching pattern within a genus) [50]. Our creation of 3-D models mainly used image-based photogrammetry modeling techniques [42] by 3ds Max and its tool of mesh smoothing.[3] The individual leaves and stems of a plant are constantly changing as it grows. Since the plant shape/architecture in three dimensions is an important parameter of a plant's phenotype. Plant architecture both reflects the adaption of a plant to environmental conditions (e.g., sun intensity, wind or water availability, etc.) [51], [52] and determines the physical, chemical, and biotic factors to which the plant is exposed (e.g., the interception of the radiation/illumination by leaves spatial distribution, as well as photosynthesis, and transpiration, etc.) [53]–[55]. In addition, a heterogeneous natural environment is composed of different spectrally behaving surfaces placed

[3]3ds Max Reference. Online. [Available]: https://download.autodesk.com/us/3dsmax/2012help/index.html
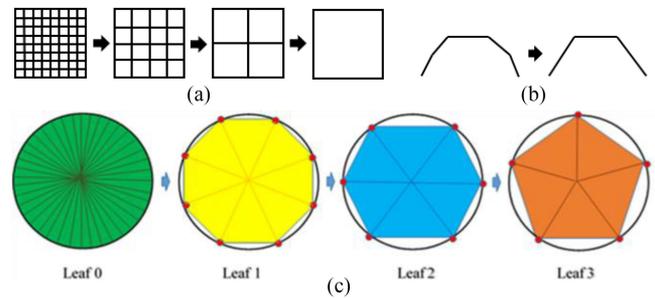

Fig. 2. Surface elements simplification rules. (a) Merging of facets. (b) Move of corners. (c) Change of key feature points (red point) on an assumed circle flat shaped leaf. Leaf 0 is the high-precision initial object. Its simplification with increasing simplification levels leads to Leaf1, Leaf2, and Leaf3.

into the 3-D space according to a specific geometry. In the computer simulation process, such a complex environment can be represented by a virtual 3-D scene assembled from various geometrical primitives (triangles, cylinders, and spheres) [5], [56], [57] that specify the optical properties of each surface [58]. If the 3-D structure of a particular morphological plant can be described explicitly, then it is possible to use models of canopy scattering behavior to describe the radiometric response of such a canopy in optical domains. A realistic description of plant and canopy architecture is essential for improving parameter retrieval from remote sensing data and achieving accurate simulation results, at least to justify the use of the turbid assumption. Here, we aimed to conserve the morphology of the two plant species during the stage of 3-D plant modeling. Both *P. australis* and *S. alterniflora* belong to Poaceae. Conversely to trees, their leaves are few, long, and curved. This curvature explains that in order to keep the leaf's basic morphology, each leaf must be simulated with several flat facets that form a curved surface. This rule is applied for all simplified 3-D objects, including the most simplified in order to simulate realistic leaf shapes.

The simplification of a real object with perfect and smooth surface details leads to a 3-D object with simple and rough surface details. It is widely used in 3-D animation and natural scene simulation. It corresponds to an approximation since perfectly smooth surfaces objects are replaced by rough surfaces objects. Fig. 2. illustrates a few steps: facets can be merged [Fig. 2(a)], key feature points on the leaf surface (e.g., leaf tip) can slightly move [Fig. 2(b)], and corner points can disappear or appear [Fig. 2(c)]. The simplification procedure conserves the basic plant morphology of the original high-precision model. For example, the spatial positions of key feature points remain unchanged, as illustrated by Fig. 2(c) where the key feature points on a circle in the initial model remain on that circle. Therefore, the simplified *S. alterniflora* and *P. australis* models keep their specific morphology. During two successive simplified models, the number of facets per leaf is reduced by a factor "four" [Fig. 2(a)] and leaf surface curvature (i.e., polyline) becomes rougher [Fig. 2(b)]. We can note that the conservation of plant morphology implies a small loss of accuracy concerning the area of the total facet.

1) Naming rules: In order to link the process of complex ecosystems to their remote sensing, it is usually useful to represent these ecosystems with accurate and detailed 3-D plant

TABLE II
NAMING RULES OF THE HIGH-PRECISION STANDARD MODEL
AND THE SIMPLIFIED MODELS

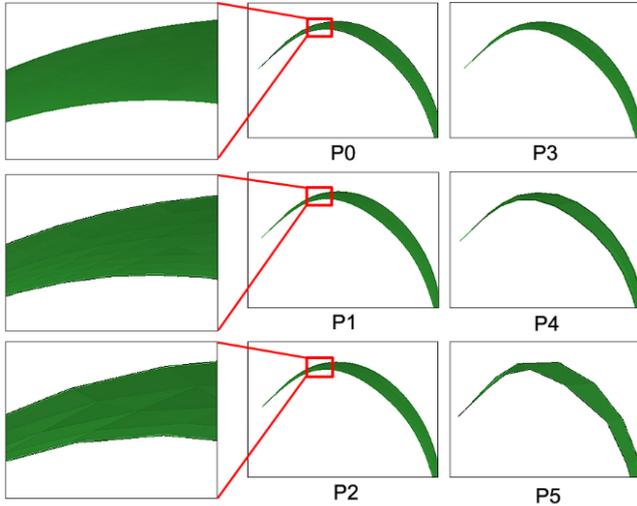| Simplified model	High-precision standard model	Simplified 1 time	Simplified 2 times	Simplified 3 times	Simplified 4 times	Simplified 5 times
P.australis model	P0	P1	P2	P3	P4	P5
S.alterniflora model	S0	S1	S2	S3	S4	S5

Fig. 3.   Change of leaf detail when simplifying the 3-D plant model from most accurate P0 to least accurate P5.

models. Table II gives the names of the plant that we used: the first letter for the species followed by an index that is "0," for the highest-precision standard 3-D model that has the largest number of facets, and the index "*n*" for the 3-D model that is simplified *n* times.

Fig. 3 illustrates the change of leaf details from the initial (i.e., most accurate) 3-D plant model P0 to the most simplified (i.e., least accurate) P5. From P0 to P5, leaf curvatures become less continuous and leaf edges become coarser. As already said (Fig. 2), the simplification procedure reduces the number of facets of 3-D plants while preserving plant morphology (i.e., key feature points). It results that the leaf area of 3-D plants changes. If the strategy had been to conserve the leaf area of plants, then plant morphology would have been much less well preserved.

B.   Scene Modeling

1) Parameters Setting in DART: DART used the 3-D objects mentioned above and their geometric distribution to create realistic landscape mock-ups. Each mock-up was defined by two parameters: DART cell and scene dimensions. The scene dimension was set to 1.0 m × 1.0 m with variable cell dimensions from 0.01 to 0.05 m with a step equal to 0.02 m, as shown in Table III.

Because it greatly affects canopy reflectance, canopy heterogeneity is a major source of parameter retrieval error in

TABLE III
DART CELL DIMENSIONS IN THE 1 M × 1 M DART SCENE

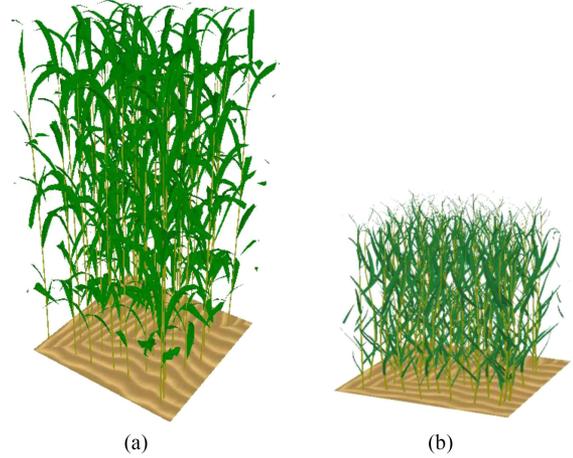| Cell dimensions	x and y [m]	0.01	0.03	0.05
	z [m]	0.01	0.03	0.05

Fig. 4.   Display of two DART scenarios for *P. australis* (a) and *S. alterniflora* (b).

TABLE IV
BAND SETTING

Spectral band1	Central wavelength [μm]	0.67
	Spectral bandwidth [μm]	0.01
Spectral band2	Central wavelength [μm]	0.8
	Spectral bandwidth [μm]	0.01

quantitative remote sensing studies. Here, we studied it with six plant densities [7] (i.e., 20, 40, 60, 80, 100, and 120 plants per m^2) in 1 m by 1 m scenes. Fig. 4 shows two examples of scenarios (i.e., DART scenes). In each scenario, all 3-D plants have the same positional (x, y) and rotation (ϕ) random features. In each scene, plant distribution follows two rules: 1) random distribution of all 3-D plants on the *XY* plane, 2) random rotation of each 3-D plant around the *Z*-axis. It gives a realistic plant distribution and eases further analyses. In all, 108 scenes were simulated per species, using six simplified 3-D plant models, six densities, and three DART cell dimensions.

DART was run with 100 discrete directions that sample the 4π space of directions, a sun zenith angle equal to 30°, a sun azimuth angle equal to 225°, and two spectral bands adapted to compute NDVI (Table IV).

C.   Canopy Reflectance and NDVI Calculation

A standard quantity [59] commonly defines surface reflectance: the BRDF. It is the ratio of the radiance leaving the surface along a direction to the surface irradiance due to an incident collimated radiation. DART uses another commonly accepted definition that can be directly measured in the field: the bidirectional reflectance factor (BRF). It is equal to the

ratio of the radiance leaving the target surface along a direction to the radiance that leaves a reference surface (i.e., white and Lambertian surface) along the same direction, the target and reference surfaces being in the same illumination configuration. Actually, BRF = $\pi \cdot$BRDF. DART simulates top of atmosphere (TOA) and bottom of atmosphere (BOA) spectral radiance and BRF images. Here, we only considered DART BOA radiance at 0.67 and 0.8 μm. A text file called BRF with three columns stores the mean values of the DART BRF images. Its first two columns store the zenith and azimuth angles of all user-defined viewing directions in the upper hemisphere, and the third column stores the BRF values.

DART was run for each parameter combination scenario with storage of computing time and computation of BOA NDVI values for all viewing directions in the upper hemisphere according to the following formula:

$$\text{NDVI} = (R\_800 - R\_670) / (R\_800 + R\_670). \quad (1)$$

IV. RESULTS AND DISCUSSION

A. Nadir NDVI

Since all scenarios were simulated with the same random position and rotation features, the only factors that influence the DART simulated BRF values are the density of plants, the degree of simplification of the 3-D plant model, and the DART cell dimensions. Here, we assume that the most detailed plant object P0 leads to the most accurate DART simulated NDVI in each cell dimension group. The dimensions of DART cells influence the accuracy of simulations. This change is very difficult to forecast because DART uses different rules when modeling leaf/facet scattering. For example, leaf scattering is simulated with at least one scattering point per cell and per facet. With this rule, the trend is that the smaller the cells and facets, the larger the number of leaf scattering points, and the more accurate the simulation. However, this trend can be easily outweighed by the fact that a facet that belongs to several cells is partitioned into several subfacets, which modifies the location of scattering points and therefore can slightly modify results. It explains why the cell dimension is treated as a variable that influences the accuracy of simulations.

Fig. 5 shows the DART *P. australis* and *S. alterniflora* NDVI for a nadir viewing direction and sun zenith angle equal to 30°, for plant density from 20 to 120 plants per m², 3-D object simplification (index from 0 to 5), and DART cell dimensions (0.01 m $\times$ 0.01 m, 0.03 m $\times$ 0.03 m, 0.05 m $\times$ 0.05 m). As expected, NDVI increases as plant density increases and converges to a constant value above a plant density limit value. Here, given the necessary inaccuracies associated to plant measurements and modeling, this plant density limit is defined by $\left| \frac{\text{NDVI}_{\text{plant density}} - \text{NDVI}_{\text{plant density increased}}}{\text{NDVI}_{\text{plant density increased}}} \right| \leq 10^{-1}$. Whatever, the level of detail of the 3-D plant model, the density limit is about 60 plants per m² for *P. australis* [Fig. 3(a)–(c)], and about 80 plants per m² for *S. alterniflora* [Fig. 5(d)–(f)]. This saturation of NDVI corresponds to the saturation of the visible and near-infrared spectral bands used to compute NDVI. Knowledge of the plant density limit can be very interesting for modeling
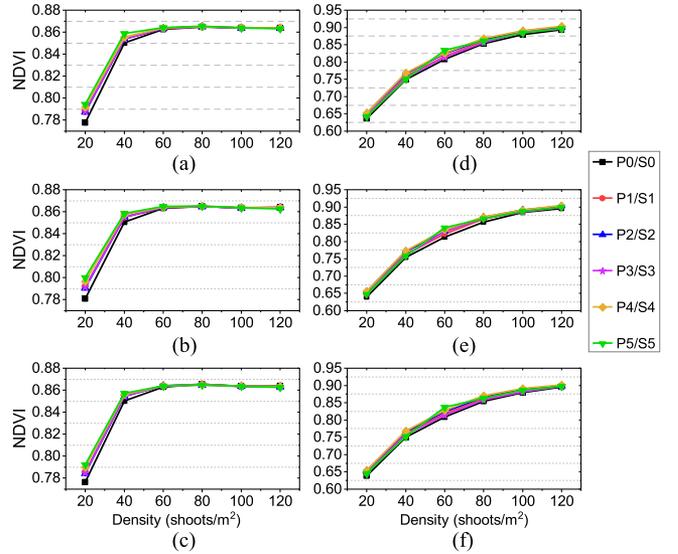

Fig. 5. DART nadir NDVI for the six simplification levels of plant 3-D objects (left: *P. australis*; right: *S. alterniflora*) and three DART cell dimensions (from top to bottom: 0.01 m $\times$ 0.01 m, 0.03 m $\times$ 0.03 m, 0.05 m $\times$ 0.05 m).

works. For example, for the simulation of NDVI, there is no need to simulate vegetation covers with a plant density higher than the plant density limit if the expected relative accuracy of NDVI is 10^{-1}. This approach can drastically reduce the number of plants that need to be simulated to get accurate simulations of radiometric measurements with a given predefined accuracy. Therefore, it can save a huge amount of computer time and memory, and consequently greatly improve the efficiency of remote-sensing-based strategies when studying vegetation with a modeling approach.

Fig. 5 illustrates that the level of simplification of the 3-D plant object can greatly influence the accuracy of the simulated NDVI of *P. australis* and *S. alterniflora* scenes that have small plant densities (i.e., plant density smaller than the plant density limit). The NDVI of the *P. australis* scenes [Fig. 5(a)–(c)] simulated with simplified 3-D plant models is always larger than the NDVI simulated with the most detailed 3-D plant model P0. It is not the case for the *S. alterniflora* scenes. Then, whatever the plant density, the NDVI simulated with simplified 3-D plant models can be larger than the NDVI simulated with the most detailed 3-D plant model S0. The relative error $\frac{\text{NDVI}_{\text{Sn}} - \text{NDVI}_{\text{S0}}}{\text{NDVI}_{\text{S0}}} \in [10^{-5}, 3.48\%]$ where NDVI_{Sn} is the NDVI of plant model Sn. It can be too large for some cases. It is mostly explained by the change of the curvature of leaves with the simplification level of the 3-D plant models.

The NDVI curves of *S. alterniflora* and *P. australis* as a function of plant density differ greatly: *P. australis* NDVI increases much faster than *S. alterniflora* NDVI. This is explained by morphological differences between the two types of plants. *P. australis* has large and boat-shaped leaves, whereas the *S. alterniflora* leaves are narrow and long. Moreover, the average height and foliage cover of each single *P. australis* plant are higher than those of *S. alterniflora*.

Compared to the influence of plant density and the simplification of the 3-D plant model, the influence of DART cell
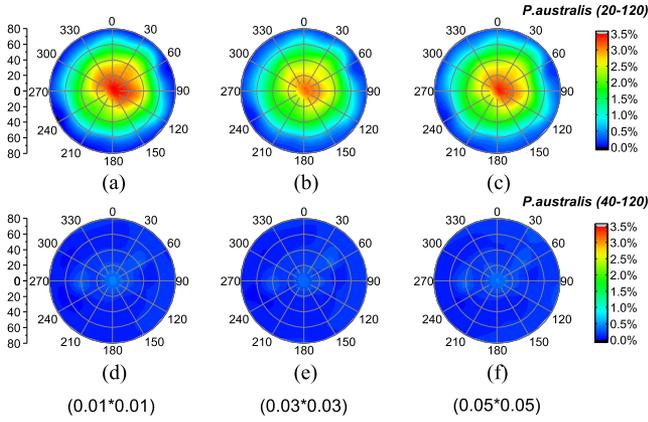
Fig. 6. Polar plots of the coefficient of variation of P. australis NDVI relative errors per upward direction (VZA: distance to center, VAA: clockwise) for three DART cell sizes. (a, d) 0.01 m × 0.01 m; (b, e) 0.03 m × 0.03 m; (c, f) 0.05 m × 0.05 m, and two plant density ranges (top: 20–120 plants/m²; bottom: 40–120 plants/m²).
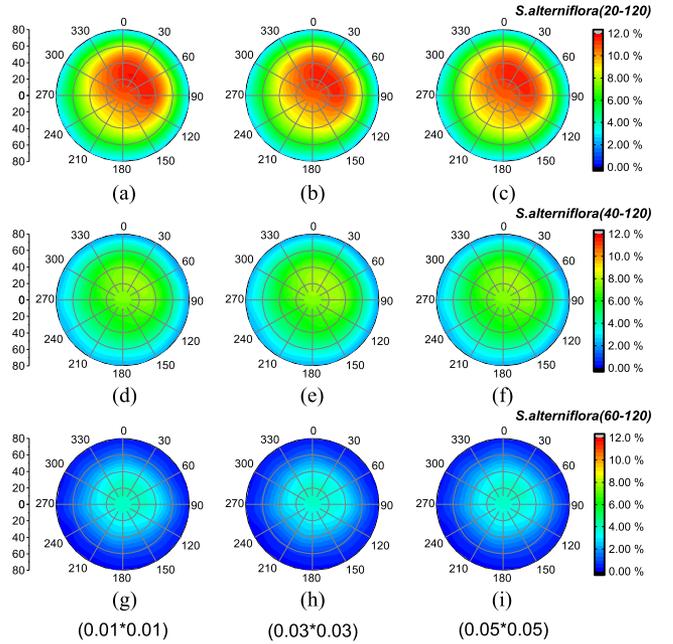

Fig. 7. Polar plots of the coefficient of variation of S. alterniflora NDVI relative errors per upward direction (VZA: distance to center, VAA: clockwise) for three DART cell sizes (a,d,g: 0.01 m × 0.01 m; b,e,h: 0.03 m × 0.03 m; c,f,i: 0.05 m × 0.05 m), and three plant density ranges (top: 20–120 plants/m²; middle: 40–120 plants/m²; bottom: 60–120 plants/m²).

dimensions is much smaller. For example, the associated maximum relative differences of NDVI for DART cells between 1 and 5 cm are less than 0.165% for P0, 0.334% for P1, 0.395% for P2, 0.393% for P3, 0.239% for P4, and 0.292% for P5; they are less than 0.194% for S0, 0.457% for S1, 0.403% for S2, 0.527% for S3, 0.362% for S4, and 0.417% for S5. Relative differences between simulations where only DART scene dimension changes are smaller.

B. Directional NDVI

Above, we only studied the nadir viewing direction. Actually, most remote sensing observations are off-nadir. For example, MODIS VZA reaches 55° [60]. This point is important because vegetation canopies are not Lambertian surfaces. For example, the albedo of a canopy with an anisotropic BRDF may be underestimated by as much as 45% if it is computed with nadir reflectance only [61]. Therefore, for each species and each DART cell dimension, we calculated the coefficient of variation for all relative errors of all parameter combinations per upward viewing direction, for a 30° SZA and 225° SAA. In Fig. 6, two groups of P. australis simulations are considered: group 1 of all P. australis simulations and group 2 of simulations with plant density larger than 20 plants/m². Group 1 has maximum relative errors up to 3.5% at nadir, with a dissymmetry toward the hot spot, and smaller values for very oblique viewing directions. Group 2 has greatly smaller relative errors, always less than 0.5%, with larger errors also at nadir. These results are observed for all DART cell dimensions. They stress that larger errors occur with smaller plant densities. Actually, a plant density as small as 20 plants/m² is not observed in the field. Therefore, below, we only consider plant densities larger or equal to 40 plants/m².

Similarly, Fig. 7 shows polar plots of the coefficient of variation of S. alterniflora NDVI relative errors per upward viewing direction for DART cell sizes equal to 0.01 m × 0.01 m, 0.03 m × 0.03 m, and 0.05 m × 0.05 m. Here, three groups are considered:

plant density 20–120 plants/m², 40–120 plants/m², and 60–120 plants/m². Relative errors are maximum for VZA < 60°. They reach 12% with plant density equal to 20 plants/m². As for P. australis NDVI, relative errors are greatly reduced if scenes with 20 plants/m² are excluded [i.e., Fig. 5(d)–(f)]. Similarly, the further exclusion of densities equal to 40 plants/m² further decreases the coefficient of variation that becomes smaller than 4%. Since in the field, plant densities are usually larger than 40 plants/m², below we only consider plant densities larger than 60 plants/m² for S. alterniflora.

C. Relative Error per Plant Density and Simplification Level

Fig. 8 shows the relative errors of P. australis NDVI results per plant density, after having excluded the lower plant density, as box plots per plant simplification level and per DART cell dimension. The relative error values vary with the n parameter combinations. The lower density of 40 plants/m² still gives the larger relative error. DART cell dimensions lead to much smaller relative errors than the plant simplification level. As already noted for the nadir viewing direction, the most simplified plant model also leads to the larger relative errors. This is true at all plant densities, including the larger plant densities. This result is not intuitive because one would have thought that the influence of the simplification level decreases if plant density increases. This highlights that despite their computational efficiency advantages, highly simplified plant models may not be acceptable, depending on the accuracy expected on simulated NDVI.
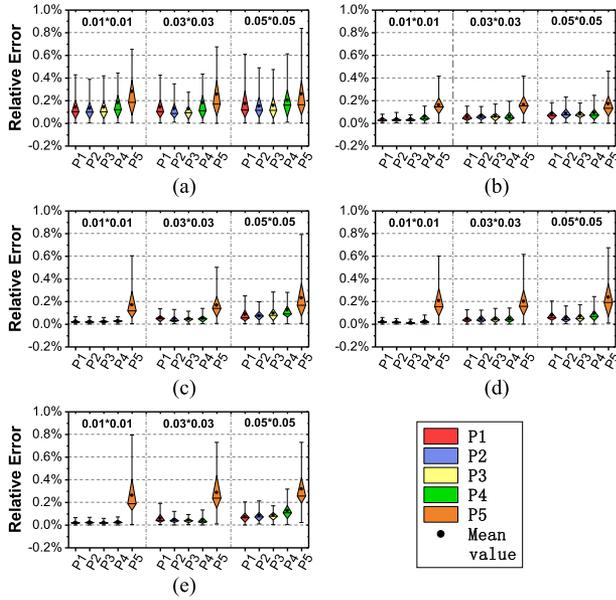
Fig. 8. Relative error of all *P. australis* simulations per group of plant density from 40 plants/m^2 (a) to 120 plants/m^2 (e), for cell dimensions equal to 0.01 m * 0.01 m, 0.03 m * 0.03 m, and 0.05 m * 0.05 m. (a) *P.australis* 40/m^2. (b) *P.australis* 60/m^2. (c) *P.australis* 80/m^2. (d) *P.australis* 100/m^2. (e) *P.australis* 120/m^2
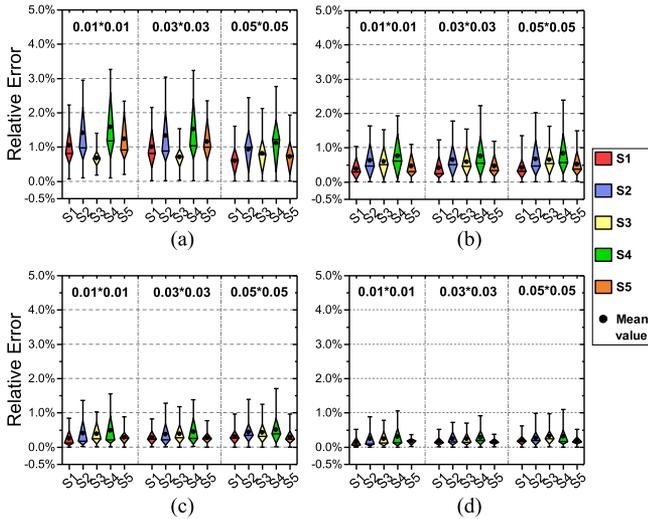

Fig. 9. Relative error of all *S.alterniflora* simulations per group of plant density from 60 plants / m^2 (a) to 120 plants / m^2 (d), for cell dimensions equal to 0.01 m * 0.01 m, 0.03 m * 0.03 m and 0.05 m * 0.05 m.

Fig. 9 shows the relative errors of *S. alterniflora* NDVI results per plant density, for plant density equal and larger to 60 plants/m^2, as box plots per plant simplification level, and per DART cell dimension. Results differ from those of *P. australis*. In particular, relative errors are about five-times higher, and there is no clear relationship between the relative error and the simplification level of *S. alterniflora*. For example, relative errors for S5 are close to those for S1 and smaller than those for S2, S3, and S4. We also can note that relative errors of *S. alterniflora* clearly decrease with the increase of plant density from 60 plants/m^2 to 120 plants/m^2, conversely to *P. australis*

Fig. 10. Scatterplot of all P. australis combinations NDVI relative errors and computer times. Symbols ☆, ∗, ∘, △, and □ represent 40, 60, 80, 100, and 120 plants/m^2, respectively. Colors represent plant simplification levels: yellow for P5, pink for P4, blue for P3, red for P2, green for P1, and black for P0. The size of symbols indicates DART cell size, with smallest size for 0.01 m * 0.01 m, medium size for 0.03 m * 0.03 m, and largest size for 0.05 m * 0.05 m.

for which relative errors remain stable if plant density increases above 60 plants/m^2. We can note an extremely small increase of the relative errors for *P. australis* and *S. alterniflora* if the dimensions of DART cells increase.

In short, for the relative errors of *P. australis*, plant density is the most influential factor between 40 plants/m^2 and 60 plants/m^2. Above 60 plants/m^2, the simplification level of plants is the most influential factor beyond the P4 level. For the relative errors of *S. alterniflora*, plant density is the most influential factor regardless of the plant density value. Plant simplification is a much less influential factor.

D. Selection of Optimal Parameters as a Function of Time Cost and NDVI Relative Error

Each of the above parameter combinations (i.e., dimensions of DART cells, level of plant simplification, and plant density) leads to DART simulation characterized by specific calculation time and relative error on the NDVI. Fig. 10 represents the scatterplot of all *P. australis* combinations NDVI relative errors and computer times obtained from a laptop with the Intel (R) Core (TM) i7- 6700HQ CPU @ 2.6GHz octa-core processor. Symbols ☆, ∗, ∘, △, and □ represent 40, 60, 80, 100, and 120 plants/m^2, respectively. Colors represent plant simplification levels: yellow for P5, pink for P4, blue for P3, red for P2, green for P1, and black for P0. The size of symbols indicates DART cell dimensions, with smallest size for 0.01 m * 0.01 m, medium size for 0.03 m * 0.03 m, and largest size for 0.05 m * 0.05 m. The analysis of Fig. 10 shows that relative errors are smaller than 20% with most of them around 5%. The longest
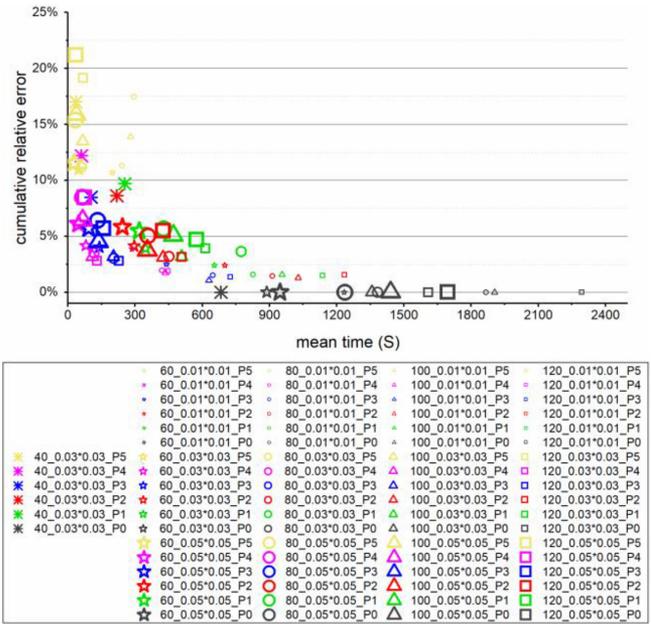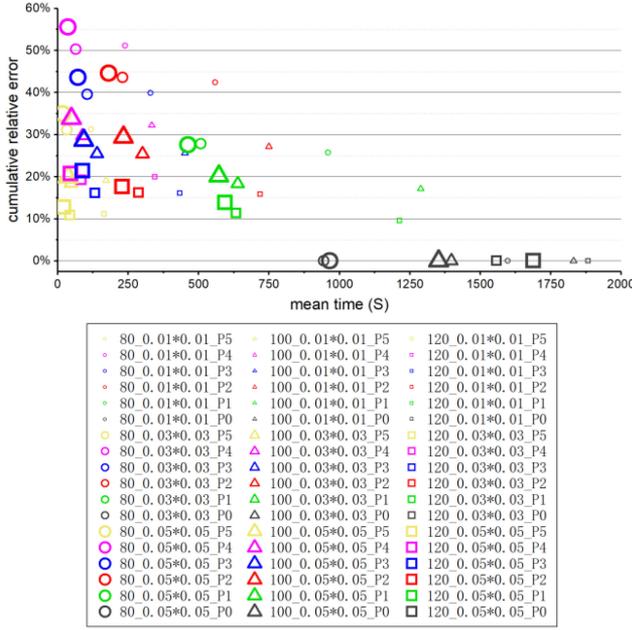
Fig. 11. Scatterplot of all P.australis combinations NDVI relative errors and computer times. Symbols ☆, ○, △, and □ represent 60, 80, 100, and 120 plants/m², respectively. Colors represent plant simplification levels: yellow for S5, pink for S4, blue for S3, red for S2, green for S1, and black for S0. The size of symbols indicates DART cell size, with smallest size for 0.01 m ∗ 0.01 m, medium size for 0.03 m ∗ 0.03 m, and largest size for 0.05 m ∗ 0.05 m.

Fig. 12. Radar map that represents the 60 combinations (red dot) of P. australis ordered according to their normalized selection index (NSI), from 0 to 0.3.

computer times are for P0. This is not surprising because P0 is the plant model with a larger number of facets, which leads to more numerous radiation interactions in the canopy. Most simplified plant models (i.e., yellow, pink, and blue symbols) correspond to the shortest computer times. In addition, smaller computer times occur for larger DART cells. Indeed, the use of large cells tends to decrease the number of radiation interactions. Computer time tends to increase with plant density, although the increase is not very large. However, Fig. 10 is not helpful as expected to determine the optimal combinations in terms of computer time and accuracy.

Fig. 11 represents the scatterplot of all *S. alterniflora* combinations NDVI relative errors and computer times (obtained from the same laptop), with colors and symbols similar to those of Fig. 10. Most values are between 10% and 40%, with extreme values of up to 55%. The fact that relative errors are more scattered than for *P. australis* eases the identification of combinations that represent the best trade-offs in terms of computer time and accuracy. However, similarly to Fig. 10, Fig. 11 still lacks universal, qualitative, and quantitative criteria for users to make decisions. Therefore, we devised the quantitative approach presented below.

First, the two quantities of interest X_i (i.e., computer time and NDVI accuracy) are normalized between 0 and 1 because they have different units:

$$X_{\text{norm}} = \frac{x_i}{\sum x_i}. \qquad (2)$$

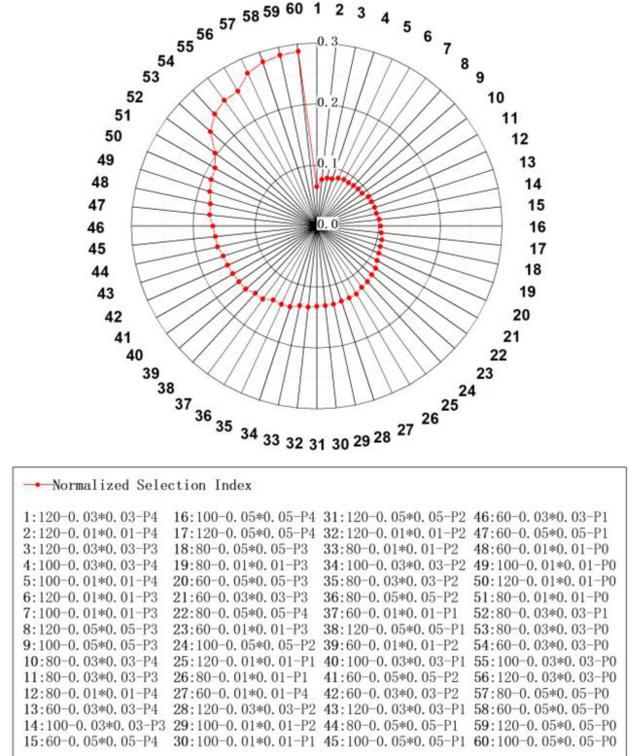Then, the normalized selection index (NSI) is defined as a linear combination of the normalized time and the normalized cumulative relative error, using two weighting factors α and β:

$$\text{NSI} = \alpha * \text{NT} + \beta * \text{NCAE}. \qquad (3)$$

The weighting factors α and β can be set by the user with $\beta = 1 - \alpha$. The larger α, the more importance is given to the computer time. Usually, this situation occurs in large-scale scene simulations at the kilometer level that does not require a high simulation results accuracy, or in scenarios composed of high-precision standard models that take up a large amount of storage memory. As for the simulation of small-scale scenes, we expect to obtain very accurate simulation results and pay more attention to the proportion of β value. Here, we selected $\alpha = \beta = 0.5$ because equal importance was given to computer time and accuracy. Fig. 12 shows the resulting NSI of *P. australis* in NSI ascending order. Combinations with P5 were excluded because they give too large relative errors. The best combination (i.e., smaller NSI) corresponds to the scene that is simulated with 120 P4 plants/m² and cell dimension of 0.03 m ∗ 0.03 m. It appears that NSI does not change linearly with the change of density, nor does it follow the simplification of 3-D objects or the cell dimension. It supports our initial assumption that the three factors involved in our analysis must be comprehensively considered in order to choose the most suitable simulation scenario. In addition, we can note that the plant density of the best 10 cases is between 100 and 120 plants/m². On the one hand, the simplified 3-D object shows better applicability compared with the high-standard precision 3-D object since the cases using P0 were ranked at the end according to NSI. On the other hand, those simulation cases
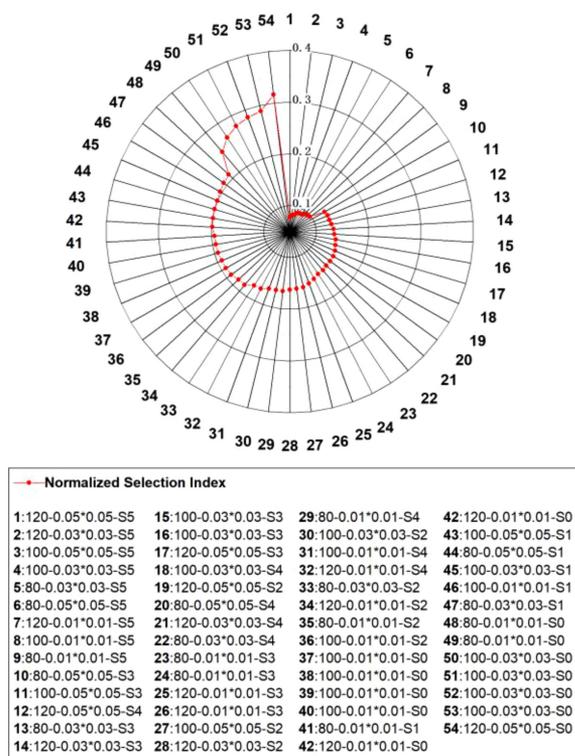
Fig. 13. Radar map that represents the 54 combinations (red dot) of *S. alterniflora* with more than 60 plants/m², ordered according to their normalized selection index (NSI), from 0 to 0.4.

Fig. 14. (a) DART color composite of the S5 plot. (b) Nadir image of S5 in the NIR. (c) Relative difference of nadir reflectance of S1, S2, S3, S4, and S5 relative to S0 in the red and NIR with a zero reflectance ground.

using 3-D objects that have been simplified more than twice were in the top half of all simulations. These two key points supported our point of view of using simplified 3-D models and consider the simulated density rather than a real density in simulation work.

Fig. 13 shows the resulting NSI of *S. alterniflora* in NSI ascending order for combinations. Combinations with 60 plants/m² are excluded because they give too large relative errors. The optimal combination is for 100–120 S5 plants/m² with a cell dimension of 0.03 m ∗ 0.03 m or 0.05 m ∗ 0.05 m. Similar to *P. australis*, the best combinations are for larger plant densities and most simplified plant models, except that the most simplified *P. australis* plant was unacceptable because it led to too large errors. We can note a difference between *S. alterniflora* and *P. australis*: the best cases are with intermediate cell dimensions for *P. australis*, and with largest cell dimensions for *S. alterniflora*.

E. Discussion

In this article, we investigated three factors that influence the computation time and NDVI accuracy of DART simulations of two plant species: DART cell dimension, level of plant simplification, and plant density. The question at hand was to determine the optimal combination of these three factors. It is an important question when one wants to simulate remote sensing acquisitions of large landscapes. First, very detailed 3-D plant objects of two-dominant plant species, *P. australis* and *S. alterniflora*, were

created using detailed *in-situ* measurements. Since too detailed plant models can need inacceptable computation times when simulating large areas [62], [63], 3-D plant models are usually simplified. However, this simplification can be a source of inaccuracy. An additional difficulty is that this inaccuracy depends on other factors such as plant density and also parameters of the RT model used to simulate the remote sensing signals. Here, the 3-D plant models were simplified to five levels each, and we considered three DART cell dimensions and six plants simulated densities, knowing that indeed, NDVI tends to saturate at large plant densities (Fig. 5).

During the investigation to determine the best trade-off in terms of computer time and accuracy, the most simplified *P. australis* plant (i.e., P5) was excluded because it led to NDVI errors much larger than P4, most probably due to an excessive abstraction of the initial P0 object. Similarly, smaller plant densities of *P. australis* and *S. alterniflora* were excluded because they led to excessively large NDVI differences compared to those of canopies with plant densities observed in the field. Indeed, NDVI tends to saturate at large plant densities (Fig. 5).

Surprisingly, the most simplified plant level of *S. alterniflora* (i.e., S5) led to results as accurate as S1 and more accurate than S2, S3, and S4. After analyzing nadir reflectance images of the S5 plot [Fig. 14(a)], we analyzed the nadir red and NIR reflectance of a single S5 plant [Fig. 14(b)] over a zero reflectance ground. It appears that the relative difference $\frac{\text{Reflectance}(Sn) - \text{Reflectance}(S0)}{\text{Reflectance}(S0)}$, with *n* from 1 to 5, is not a monotonous function of the simplification level, and that it is

minimum for S5, which explains that S5 leads to the most accurate results.

The NDVI of *S. alterniflora* and *P. australis* appeared to vary differently with their level of simplification. The most probable explanation for these differences is that these plants have different morphologies. Indeed, the blade of *S. alterniflora* is not a simple curved narrow plane, but rather a curved U-shaped roll, whereas *P. australis*'s blades are relatively wide and flat. In addition, *S. alterniflora* leaves are relatively short, thin, and narrow, whereas *P. australis* leaves are taller and larger, which leads to the different influence of the ground, even if the two types of plants have the same leaf area.

The visual analysis of the scatterplots of results (Figs. 10 and 11) did not allow a clear determination of the combinations of factors that give the best trade-off in terms of computation time and accuracy. Therefore, we designed an index (i.e., NSI) that allowed us to determine the optimal factor combinations. Given the universality and reliability of the selection criteria that we considered and the flexibility of parameters' setting in DART, our method to determine the optimal simulation parameters could be extended to any vegetation type, spectral domain, the geometric configuration of observation, and large-scale research. Plants of the Gramineae family all have similar growth architecture so the method mentioned in this article can be applied to any gramineous plants. As nongramineous plants do not necessarily share the morphological characteristics of gramineous plants, researchers need to follow the entire modeling and results in the discussion process in this article to create a series of simplified 3-D plant objects to be used for simulation scenarios and then making trade-offs and selection by analyzing nadir and directional simulation results.

V. CONCLUSION

Theoretically, the 3-D scene model will help to understand BRDF physics better over natural surfaces and it is also valuable for application in simulation of canopy RT process as well as visualization in quantitative remote sensing. In this article, we established six 3-D objects separately for *P. australis* and *S. alterniflora* with different simplification degrees based on the field measurement and made up to 108 combinations, respectively, with six kinds of simulation densities and three kinds of DART cell dimension. By analyzing the variation rule of NDVI results with density changing in different cases, we screened the suitable simulated density for the field environment simulation. In the vertical view, the *P. australis* scenarios had relatively greater coverage than *S. alterniflora*. Meanwhile, to avoid the nadir observation error, we compared the potential variability of the results of the lower simulated density in other directions in the hemispherical space, and further confirmed the inapplicability of the lower simulated density. The cumulative relative error indicated that all the most simplified 3-D objects were not applicable for our studies and can be eliminated since their severe distortion during the simplification process. Then, we proposed confident criteria for evaluation and parameter selection via

analyzing the simulation relative error of NDVI and the efficiency of time cost. Two satisfying parameter combinations were also obtained from the selection criteria (Figs. 12 and 13) for further researches of *P. australis* and *S. alterniflora* in more complex scenario simulations. Compared with other group combinations, the most appropriate case for each species showed the minimum NSI when we assumed as users giving both the α and β the value of 0.5. The influence degree of simulated density, 3-D objects precision, and DART cell dimension can be roughly ranked as simulated density$>$3-D objects precision$>$DART cell dimension. In some cases, the cell dimension was more of an impact on the computing time. A general conclusion is that it is necessary to consider botanical morphology precision and the most optimized simulated density when simulating vegetation. The new indices of the NSI we designed can be determined by focusing on the weight setting of the α and β coefficients according to the actual requirements of the user. The NSI is a major result of this article. It is expected to be very helpful for the future study of simulating a large-scale space range vegetation landscape and worthy of further study applying to very complex vegetation scenarios.

APPENDIX

TABLE A1
EXAMPLES OF PLANT HEIGHT, LEAF NUMBER, AND BASE RHIZOME WIDTH

Number	Height (cm)	Base rhizome width (cm)	Leaf number
P1	128	0.492	9
P2	121	0.580	10
P3	109	0.300	6
P4	115	0.644	8
P5	125	0.550	9
P6	120	0.360	9
P7	122	0.270	8
P8	105	0.570	9
P9	70	0.286	11
P10	80	0.362	12
P11	74	0.420	11
P12	82	0.274	8
P13	102	0.298	8
P14	105	0.380	9
P15	110	0.308	11
P16	98	0.530	9
P17	90	0.358	9
P18	84	0.508	8
P19	110	0.562	8
P20	88	0.318	4
P21	112	0.408	10
P22	113	0.462	10
P23	100	0.344	9
P24	82	0.390	9
P25	84	0.500	9
Average	101.16	0.41896	8.92

TABLE A2
EXAMPLES OF LEAF LENGTH, LEAF WIDTH, AND LEAF SPACING

Number	Length (cm)	Width (cm)	Spacing (cm)	Length (cm)	Width (cm)	Spacing (cm)	Length (cm)	Width (cm)	Spacing (cm)
P1	21.5	1.3	12.3	25.5	1.3	6.7	26.7	1.5	6.5
P2	35.8	1.4	6.4	35.9	1.3	5.9	39.5	1.4	4.3
P3	26.6	1.4	8.5	30.8	1.5	7.2	32.4	1.4	6.4
P4	32.5	1.4	5.7	31.8	1.6	12.2	23.5	1.6	5.4
P5	27.3	1.4	9.8	34.1	1.4	6.9	33.2	1.4	8.9
P6	30.1	1.4	9.5	33.8	1.4	7.3	35.1	1.3	6.4
P7	28.3	1.3	9.4	30.4	1.3	6.3	30.2	1.3	6.3
P8	32.1	1.4	7.3	31.4	1.4	7.4	35.2	1.5	5.3
P9	7.1	1.5	14.6	24.6	1.8	13.2	30.9	2.1	7.4
P10	11.3	1.3	15.1	20.4	1.3	10.5	25.6	1.4	10.6
P11	9.2	0.8	16.1	19.6	1.2	14.4	27.4	1.4	12.5
P12	16.1	1.1	4.5	25.4	1.4	12.2	30.8	1.8	9.6
P13	25.1	1.3	11.1	29.5	1.5	9.2	35.6	1.8	9.2
P14	18.3	1.4	10.1	25.8	1.6	10.2	36.5	1.6	8.6
P15	29.5	1.5	19.7	34.4	1.5	9.5	38.5	1.5	8.5
P16	19.2	1.4	6.3	26.1	1.5	9.8	30.2	1.6	9.3
S1	28.4	0.7	4.1	30.6	0.9	4.6	39.4	0.9	2.7
S2	6.1	0.5	2.8	10.1	0.7	3.1	17.2	0.9	8.2
S3	30.2	1	5.4	33.7	0.9	4.9	37.6	0.8	4.3
S4	29.4	1.4	8.6	32.8	1.4	7.8	32.2	1.6	9.4
S5	33.1	1.2	12.1	41.3	1.3	7.2	47.5	1.2	8.1
S6	20.9	1.2	10.1	24.8	1.1	10.7	34.5	1.1	3.5
S7	27.4	0.8	4.7	32.1	0.9	8.6	33.8	0.9	8.3
S8	15.4	0.9	1.2	21.8	1.1	3.4	27.2	0.9	10.7
S9	21.1	1	4.1	25.6	1.1	5.4	28.2	0.9	7.9
S10	30.2	0.8	5.4	33.2	0.6	5.3	34.6	0.9	6.1
S11	24.3	0.9	7.5	32.6	0.8	5.6	37.4	0.9	3.9
S12	31.1	0.9	9.5	31.2	0.9	8.5	32.5	0.7	6.4
S13	27.6	0.5	3.6	34.1	0.8	4.5	41.6	0.9	3.1
S14	7.1	1	7.6	33.4	1	5.2	38.2	0.9	1.5
S15	34.1	1.1	7.7	36.7	1	9.5	39.8	1.1	11.1
S16	20.6	0.9	9.3	30.6	1	6.6	41.2	1.1	0.9

TABLE A3
AVERAGE COMPUTATION TIME OF *P. AUSTRALIS* SIMULATION CASES

Simulation cases	Mean time (s)	Simulation cases	Mean time (s)	Simulation cases	Mean time (s)
20-0.01*0.01-P5	93.0	20-0.03*0.03-P5	22.0	20-0.05*0.05-P5	12.0
20-0.01*0.01-P4	118.0	20-0.03*0.03-P4	34.0	20-0.05*0.05-P4	19.0
20-0.01*0.01-P3	171.0	20-0.03*0.03-P3	57.0	20-0.05*0.05-P3	39.0
20-0.01*0.01-P2	287.0	20-0.03*0.03-P2	118.0	20-0.05*0.05-P2	96.0
20-0.01*0.01-P1	259.0	20-0.03*0.03-P1	138.0	20-0.05*0.05-P1	127.0
20-0.01*0.01-P0	469.0	20-0.03*0.03-P0	348.0	20-0.05*0.05-P0	359.0
40-0.01*0.01-P5	151.0	40-0.03*0.03-P5	36.0	40-0.05*0.05-P5	21.0
40-0.01*0.01-P4	212.0	40-0.03*0.03-P4	59.0	40-0.05*0.05-P4	36.0
40-0.01*0.01-P3	318.0	40-0.03*0.03-P3	103.0	40-0.05*0.05-P3	70.0
40-0.01*0.01-P2	532.0	40-0.03*0.03-P2	218.0	40-0.05*0.05-P2	175.0
40-0.01*0.01-P1	478.0	40-0.03*0.03-P1	253.0	40-0.05*0.05-P1	228.0
40-0.01*0.01-P0	681.0	40-0.03*0.03-P0	683.0	40-0.05*0.05-P0	674.0
60-0.01*0.01-P5	198.0	60-0.03*0.03-P5	48.0	60-0.05*0.05-P5	27.0
60-0.01*0.01-P4	286.0	60-0.03*0.03-P4	80.0	60-0.05*0.05-P4	47.0
60-0.01*0.01-P3	440.0	60-0.03*0.03-P3	140.0	60-0.05*0.05-P3	93.0
60-0.01*0.01-P2	700.0	60-0.03*0.03-P2	296.0	60-0.05*0.05-P2	243.0
60-0.01*0.01-P1	654.0	60-0.03*0.03-P1	346.0	60-0.05*0.05-P1	318.0
60-0.01*0.01-P0	1233.0	60-0.03*0.03-P0	888.0	60-0.05*0.05-P0	946.0
80-0.01*0.01-P5	241.0	80-0.03*0.03-P5	61.0	80-0.05*0.05-P5	34.0
80-0.01*0.01-P4	418.8	80-0.03*0.03-P4	117.0	80-0.05*0.05-P4	65.0
80-0.01*0.01-P3	647.5	80-0.03*0.03-P3	204.0	80-0.05*0.05-P3	132.0
80-0.01*0.01-P2	913.3	80-0.03*0.03-P2	452.0	80-0.05*0.05-P2	357.0
80-0.01*0.01-P1	826.0	80-0.03*0.03-P1	773.7	80-0.05*0.05-P1	428.0
80-0.01*0.01-P0	1867.0	80-0.03*0.03-P0	1383.0	80-0.05*0.05-P0	1236.5
100-0.01*0.01-P5	280.0	100-0.03*0.03-P5	66.0	100-0.05*0.05-P5	37.0
100-0.01*0.01-P4	435.7	100-0.03*0.03-P4	109.0	100-0.05*0.05-P4	66.0
100-0.01*0.01-P3	630.0	100-0.03*0.03-P3	203.0	100-0.05*0.05-P3	136.5
100-0.01*0.01-P2	1028.0	100-0.03*0.03-P2	424.0	100-0.05*0.05-P2	354.0
100-0.01*0.01-P1	956.0	100-0.03*0.03-P1	507.0	100-0.05*0.05-P1	470.0
100-0.01*0.01-P0	1905.0	100-0.03*0.03-P0	1357.0	100-0.05*0.05-P0	1441.0
120-0.01*0.01-P5	296.0	120-0.03*0.03-P5	67.0	120-0.05*0.05-P5	36.0
120-0.01*0.01-P4	446.0	120-0.03*0.03-P4	129.0	120-0.05*0.05-P4	74.0
120-0.01*0.01-P3	725.0	120-0.03*0.03-P3	227.0	120-0.05*0.05-P3	159.0
120-0.01*0.01-P2	1235.0	120-0.03*0.03-P2	507.0	120-0.05*0.05-P2	425.0
120-0.01*0.01-P1	1137.0	120-0.03*0.03-P1	614.0	120-0.05*0.05-P1	574.0
120-0.01*0.01-P0	2294.0	120-0.03*0.03-P0	1608.0	120-0.05*0.05-P0	1696.0

TABLE A4
AVERAGE COMPUTING TIME OF *S. ALTERNIFLORA* SIMULATION CASES

Simulation cases	Mean time (s)	Simulation cases	Mean time (s)	Simulation cases	Mean time (s)
20-0.01*0.01-S5	39.8	20-0.03*0.03-S5	11.0	20-0.05*0.05-S5	7.3
20-0.01*0.01-S4	75.5	20-0.03*0.03-S4	21.3	20-0.05*0.05-S4	13.0
20-0.01*0.01-S3	93.5	20-0.03*0.03-S3	30.5	20-0.05*0.05-S3	21.8
20-0.01*0.01-S2	160.5	20-0.03*0.03-S2	61.8	20-0.05*0.05-S2	48.0
20-0.01*0.01-S1	254.0	20-0.03*0.03-S1	125.3	20-0.05*0.05-S1	111.0
20-0.01*0.01-S0	368.0	20-0.03*0.03-S0	217.3	20-0.05*0.05-S0	224.0
40-0.01*0.01-S5	65.3	40-0.03*0.03-S5	19.0	40-0.05*0.05-S5	11.3
40-0.01*0.01-S4	126.0	40-0.03*0.03-S4	37.0	40-0.05*0.05-S4	22.3
40-0.01*0.01-S3	244.0	40-0.03*0.03-S3	56.8	40-0.05*0.05-S3	39.0
40-0.01*0.01-S2	285.5	40-0.03*0.03-S2	116.7	40-0.05*0.05-S2	91.0
40-0.01*0.01-S1	492.3	40-0.03*0.03-S1	243.5	40-0.05*0.05-S1	215.5
40-0.01*0.01-S0	753.8	40-0.03*0.03-S0	460.0	40-0.05*0.05-S0	447.3
60-0.01*0.01-S5	89.0	60-0.03*0.03-S5	25.5	60-0.05*0.05-S5	14.7
60-0.01*0.01-S4	180.0	60-0.03*0.03-S4	50.0	60-0.05*0.05-S4	29.7
60-0.01*0.01-S3	242.0	60-0.03*0.03-S3	80.3	60-0.05*0.05-S3	54.0
60-0.01*0.01-S2	417.0	60-0.03*0.03-S2	166.8	60-0.05*0.05-S2	133.7
60-0.01*0.01-S1	720.5	60-0.03*0.03-S1	371.3	60-0.05*0.05-S1	339.3
60-0.01*0.01-S0	1114.2	60-0.03*0.03-S0	705.0	60-0.05*0.05-S0	703.3
80-0.01*0.01-S5	118.5	80-0.03*0.03-S5	33.0	80-0.05*0.05-S5	18.0
80-0.01*0.01-S4	239.0	80-0.03*0.03-S4	64.3	80-0.05*0.05-S4	36.7
80-0.01*0.01-S3	329.3	80-0.03*0.03-S3	105.0	80-0.05*0.05-S3	71.5
80-0.01*0.01-S2	558.5	80-0.03*0.03-S2	230.5	80-0.05*0.05-S2	181.5
80-0.01*0.01-S1	959.5	80-0.03*0.03-S1	508.0	80-0.05*0.05-S1	462.5
80-0.01*0.01-S0	1597.0	80-0.03*0.03-S0	944.0	80-0.05*0.05-S0	966.0
100-0.01*0.01-S5	171.5	100-0.03*0.03-S5	47.0	100-0.05*0.05-S5	37.5
100-0.01*0.01-S4	334.0	100-0.03*0.03-S4	88.0	100-0.05*0.05-S4	49.0
100-0.01*0.01-S3	451.5	100-0.03*0.03-S3	139.3	100-0.05*0.05-S3	92.3
100-0.01*0.01-S2	750.0	100-0.03*0.03-S2	301.0	100-0.05*0.05-S2	233.5
100-0.01*0.01-S1	1289.0	100-0.03*0.03-S1	639.0	100-0.05*0.05-S1	572.0
100-0.01*0.01-S0	2631.0	100-0.03*0.03-S0	1397.0	100-0.05*0.05-S0	1352.0
120-0.01*0.01-S5	164.3	120-0.03*0.03-S5	44.0	120-0.05*0.05-S5	21.7
120-0.01*0.01-S4	344.0	120-0.03*0.03-S4	84.0	120-0.05*0.05-S4	47.0
120-0.01*0.01-S3	432.7	120-0.03*0.03-S3	132.3	120-0.05*0.05-S3	89.0
120-0.01*0.01-S2	718.0	120-0.03*0.03-S2	287.0	120-0.05*0.05-S2	229.7
120-0.01*0.01-S1	1213.0	120-0.03*0.03-S1	633.5	120-0.05*0.05-S1	594.0
120-0.01*0.01-S0	1882.0	120-0.03*0.03-S0	1558.0	120-0.05*0.05-S0	1688.5

REFERENCES

[1] Y. J. Yao, Q. H. Liu, Q. Liu, and X. W. Li, "LAI retrieval and uncertainty evaluations for typical row-planted crops at different growth stages," *Remote Sens. Environ.*, vol. 112, no. 1, pp. 94–106, Jan. 2008.

[2] L. F. Chen, Z. L. Li, Q. H. Liu, and X. R. Xu, "The new definition of effective emissivity of non-isothermal rough surface and its approximate expression for continuous canopy vegetation," in *Proc. IEEE Int. Geosci. Remote Sens. Symp.*, 2002, pp. 3545–3547.

[3] T. Yu *et al.*, "Modeling directional brightness temperature over a maize canopy in row structure," *IEEE Trans. Geosci. Remote Sens.*, vol. 42, no. 10, pp. 2290–2304, Oct. 2004.

[4] L. M. Zhao, X. F. Gu, T. Yu, W. Wan, L. Zhang, and Y. H. Xie, "A directional thermal radiance model for multiple scattering over surfaces," *J. Infrared Millimeter Waves*, vol. 31, no. 6, pp. 528–535, 2012.

[5] P. Lewis, "Three-dimensional plant modelling for remote sensing simulation studies using the botanical plant modelling system," *Agronomie*, vol. 19, no. 3/4, pp. 185–210, 1999.

[6] G. Simioni, J. Gignoux, and X. L. Roux, "Tree layer spatial structure can affect savanna production and water budget: Results of a 3-D model," *Ecology*, vol. 84, no. 7, pp. 1879–1894, 2003.

[7] Z. Tao, R. H. Shi, Y. Y. Zeng, and W. Gao, "Effects of distribution density and cell dimension of 3D vegetation model on canopy NDVI simulation base on DART," in *Remote Sensing and Modeling of Ecosystems for Sustainability XIV*, vol. 10405. Bellingham, WA, USA: International Society for Optics and Photonics, 2017.

[8] Q. H. Liu, X. Z. Xin, P. Tang, J. J. Liao, and B. F. Wu, *Research on Quantitative Remote Sensing Model, Application and Uncertainty*. Beijing, China: Science Press, 2010.

[9] S. B. Wu *et al.*, "Modeling discrete forest anisotropic reflectance over a sloped surface with an extended GOMS and SAIL model," *IEEE Trans. Geosci. Remote Sens.*, vol. 57, no. 2, pp. 944–957, Feb. 2019.

[10] R. B. Myneni, G. Asrar, and F. G. Hall, "A three-dimensional radiative transfer method for optical remote sensing of vegetated land surfaces," *Remote Sens. Environ.*, vol. 41, no. 2/3, pp. 105–121, 1992.

[11] Z. T. Jiao *et al.*, "An algorithm for the retrieval of the clumping index (CI) from the MODIS BRDF product using an adjusted version of the Kernel-driven BRDF model," *Remote Sens. Environ.*, vol. 209, pp. 594–611, 2018.

[12] J. Pisek *et al.*, "Data synergy between leaf area index and clumping index earth observation products using photon recollision probability theory," *Remote Sens. Environ.*, vol. 215, pp. 1–6, 2018.

[13] B. D. Xu *et al.*, "An integrated method for validating long-term leaf area index products using global networks of site-based measurements," *Remote Sens. Environ.*, vol. 209, pp. 134–151, 2018.

[14] K. Yan *et al.*, "Generating global products of LAI and FPAR from SNPP-VIIRS data: Theoretical background and implementation," *IEEE Trans. Geosci. Remote Sens.*, vol. 56, no. 4, pp. 2119–2137, Apr. 2018.

[15] K. Hasegawa, H. Matsuyama, H. Tsuzuki, and T. Sweda, "Improving the estimation of leaf area index by using remotely sensed NDVI with BRDF signatures," *Remote Sens. Environ.*, vol. 114, no. 3, pp. 514–519, 2010.

[16] Y. L. Zeng *et al.*, "An iterative BRDF/NDVI inversion algorithm based on a posteriori variance estimation of observation errors," *IEEE Trans. Geosci. Remote Sens.*, vol. 54, no. 11, pp. 6481–6496, Nov. 2016.

[17] J.-L. Roujean, J. Leon-Tavares, B. Smets, P. Claes, F. Camacho De Coca, and J. Sanchez-Zapero, "Surface albedo and toc-r 300 m products from PROBA-V instrument in the framework of Copernicus Global Land Service," *Remote Sens. Environ.*, vol. 215, pp. 57–73, 2018.

[18] Z. S. Wang, C. B. Schaaf, Q. S. Sun, Y. M. Shuai, and M. O. Román, "Capturing rapid land surface dynamics with collection V006 MODIS BRDF/NBAR/Albedo (MCD43) products," *Remote Sens. Environ.*, vol. 207, pp. 50–64, 2018.

[19] P. J. Zarco-Tejada, C. Rueda, and S. L. Ustin, "Water content estimation in vegetation with MODIS reflectance data and model inversion methods," *Remote Sens. Environ.*, vol. 85, no. 1, pp. 109–124, 2003.

[20] R. Houborg, H. Soegaard, and E. Boegh, "Combining vegetation index and model inversion methods for the extraction of key vegetation biophysical parameters using terra and aqua MODIS reflectance data," *Remote Sens. Environ.*, vol. 106, no. 1, pp. 39–58, 2007.

[21] R. Houborg and E. Boegh, "Mapping leaf chlorophyll and leaf area index using inverse and forward canopy reflectance modeling and SPOT reflectance data," *Remote Sens. Environ.*, vol. 112, no. 1, pp. 186–202, 2008.

[22] R. Pedrós, Y. Goulas, S. Jacquemoud, J. Louis, and I. Moya, "FluorMODleaf: A new leaf fluorescence emission model based on the PROSPECT model," *Remote Sens. Environ.*, vol. 114, no. 1, pp. 155–167, 2010.

[23] R. Houborg, M. C. Anderson, C. S. T. Daughtry, W. P. Kustas, and M. Rodell, "Using leaf chlorophyll to parameterize light-use-efficiency within a thermal-based carbon, water and energy exchange model," *Remote Sens. Environ.*, vol. 115, no. 7, pp. 1694–1705, 2011.

[24] W. L. Fan, J. M. Chen, W. M. Ju, and G. L. Zhu, "GOST: A geometric-optical model for sloping terrains," *IEEE Trans. Geosci. Remote Sens.*, vol. 52, no. 9, pp. 5469–5482, Sep. 2014.

[25] W. L. Fan, J. M. Chen, W. M. Ju, and N. Nesbitt, "Hybrid geometric optical–radiative transfer model suitable for forests on slopes," *IEEE Trans. Geosci. Remote Sens.*, vol. 52, no. 9, pp. 5579–5586, Sep. 2014.

[26] G. F. Yin, A. N. Li, W. Zhao, H. A. Jin, J. H. Bian, and S. B. Wu, "Modeling canopy reflectance over sloping terrain based on path length correction," *IEEE Trans. Geosci. Remote Sens.*, vol. 55, no. 8, pp. 4597–4609, Aug. 2017.

[27] D. L. Hao *et al.*, "Modeling anisotropic reflectance over composite sloping terrain," *IEEE Trans. Geosci. Remote Sens.*, vol. 56, no. 7, pp. 3903–3923, Jul. 2018.

[28] W. H. Qin and S. A. W. Gerstl, "3-D scene modeling of semidesert vegetation cover and its radiation regime," *Remote Sens. Environ.*, vol. 74, no. 1, pp. 145–162, 2000.

[29] P. Syren, "Reflectance anisotropy for nadir observations of coniferous forest canopies," *Remote Sens. Environ.*, vol. 49, no. 1, pp. 72–80, 1994.

[30] J.-P. Gastellu-Etchegorry *et al.*, "Modeling BRF and radiation regime of boreal and tropical forests I. BRF," *Remote Sens. Environ.*, vol. 68, no. 3, pp. 281–316, 1999.

[31] J.-P. Gastellu-Etchegorry *et al.*, "Discrete anisotropic radiative transfer (DART 5) for modeling airborne and satellite spectroradiometer and LIDAR acquisitions of natural and urban landscapes," *Remote Sens.*, vol. 7, no. 2, pp. 1667–1701, 2015.

[32] J.-P. Gastellu-Etchegorry *et al.*, "Simulation of satellite, airborne and terrestrial LiDAR with DART (I): Waveform simulation with quasi-Monte Carlo ray tracing," *Remote Sens. Environ.*, vol. 184, pp. 418–435, 2016.

[33] P. Guillevic, J.-P. Gastellu-Etchegorry, J. Demarty, and L. Prévot, "Thermal infrared radiative transfer within 3-D vegetation cover," *J. Geophys. Res.*, vol. 108, no. D8, pp. ACL6.1–ACL6.13, 2003.

[34] J. A. Sobrino, C. Mattar, J.-P. Gastellu-Etchegorry, J.-C. Jiménez-Muñoz, and E. Grau, "Evaluation of the DART 3D model in the thermal domain using satellite/airborne imagery and ground-based measurements," *Int. J. Remote Sens.*, vol. 32, no. 22, pp. 7453–7477, 2011.

[35] P. C. Guillevic *et al.*, "Directional viewing effects on satellite land surface temperature products over sparse vegetation canopies—A multisensor analysis," *IEEE Geosci. Remote Sens. Lett.*, vol. 10, no. 6, pp. 1464–1468, Nov. 2013.

[36] Y. Wang, N. Lauret, and J. P. Gastellu-Etchegorry, "DART radiative transfer modelling for sloping landscapes," *Remote Sens. Environ.*, vol. 247, 2020, Art. no. 111902.

[37] P. Prusinkiewicz, A. Lindenmayer, and J. Hanan, "Development models of herbaceous plants for computer imagery purposes," in *Proc. 15th Annu. Conf. Comput. Graph. Interactive Techn.*, 1988, pp. 141–150.

[38] I. Shlyakhter, M. Rozenoer, J. Dorsey, and S. Teller, "Reconstructing 3D tree models from instrumented photographs," *IEEE Comput. Graph. Appl.*, vol. 21, no. 1, pp. 53–61, May/Jun. 2001.

[39] F. Anastacio, P. Prusinkiewicz, and M. C. Sousa, "Sketch-based parameterization of L-systems using illustration-inspired construction lines and depth modulation," *Comput. Graph.*, vol. 33, no. 4, pp. 440–451, 2009.

[40] P. Prusinkiewicz and A. Lindenmayer, *The Algorithmic Beauty of Plants*. New York, NY, USA: Springer, 1990.

[41] M. Okabe, S. Owada, and T. Igarashi, "Interactive design of botanical trees using freehand sketches and example-based editing," *Comput. Graph. Forum*, vol. 24, no. 3, pp. 478–496, 2006.

[42] P. Tan, T. Fang, J. X. Xiao, P. Zhao, and L. Quan, "Single image tree modeling," *ACM Trans. Graph.*, vol. 27, no. 5, pp. 1–7, 2008.

[43] J. Liu, X. P. Zhang, and H. J. Li, "Sketch-based tree modeling by distribution control on planes," in *Proc. 9th ACM SIGGRAPH Conf. Virtual-Reality Continuum Appl. Ind.*, 2010, pp. 185–190.

[44] Y. S. Wang, H. Weinacker, and B. Koch, "A lidar point cloud based procedure for vertical canopy structure analysis and 3D single tree modelling in forest," *Sensors*, vol. 8, no. 6, pp. 3938–3951, Jun. 2008.

[45] C. Zhu, X. P. Zhang, B. G. Hu, and M. Jaeger, "Reconstruction of tree crown shape from scanned data," in *Proc. Int. Conf. Technol. E-Learn. Digit. Entertainment*, 2008, pp. 745–756.

[46] C. H. Teng, Y. S. Chen, and W. H. Hsu, "Constructing a 3D trunk model from two images," *Graph. Models*, vol. 69, no. 1, pp. 33–56, 2007.

[47] C.-H. Teng and Y.-S. Chen, "Image-based tree modeling from a few images with very narrow viewing range," *Vis. Comput.*, vol. 25, no. 4, pp. 297–307, 2009.

[48] T. Lillesand and R. Kiefer, "Remote sensing and image interpretation," *Geological J.*, vol. 30, no. 2, 1994, Art. no. 750.

[49] C. H. Wang, "Effects of environmental variation on growth, distribution of and interspecific interactions among dominant marsh plants at chongming dongtan," Ph.D. thesis, School of Life Sciences, Fudan University, Shanghai, China, 2009.

[50] A. Muhar, "Three-dimensional modelling and visualisation of vegetation for landscape simulation," *Landscape Urban Planning*, vol. 54, no. 1–4, pp. 5–17, 2001.

[51] T. Fourcaud, X. P. Zhang, A. Stokes, H. Lambers, and C. Körner, "Plant growth modelling and applications: The increasing importance of plant architecture in growth models," *Ann. Botany*, vol. 101, no. 8, pp. 1053–1063, 2008.

[52] K. Omasa, F. Hosoi, and A. Konishi, "3D lidar imaging for detecting and understanding plant responses and canopy structure," *J. Exp. Botany*, vol. 58, no. 4, pp. 881–898, 2007.

[53] P. A. Wilson and S. Chakrabrty, "The virtual plant: A new tool for the study and management of plant diseases," *Crop Protection*, vol. 17, no. 3, pp. 231–239, 1998.

[54] J. S. Hanan and P. M. Room, "Practical aspects of virtual plant research," in *Plants to Ecosystems—Advances in Computational Life Sciences*. Canberra, ACT, Australia: CSIRO, 1997, pp. 28–44.

[55] P. M. Room, L. Maillette, and J. S. Hanan, "Module and metamer dynamics and virtual plants," in *Advances in Ecological Research*, vol. 25, M. Begon and A. H. Fitter Eds. Cambridge, MA, USA: Academic Press, 1994, pp. 105–157.

[56] M. A. L. España, F. Baret, F. Aries, M. Chelle, B. Andrieu, and L. Prévot, "Modeling maize canopy 3D architecture: Application to reflectance simulation," *Ecological Model.*, vol. 122, no. 1/2, pp. 25–43, 1999.

[57] D. Luquet, A. Bégué, J. Dauzat, Y. Nouvellon, and H. Rey, "Effect of the vegetation clumping on the BRDF of a semi-arid grassland: Comparison of the SAIL model and ray tracing method applied to a 3D computerized vegetation canopy," in *Proc. IEEE Int. Symp. Geosci. Remote Sens.*, 1998, pp. 791–793.

[58] T. Dornbusch, P. Wernecke, and W. Diepenbrock, "A method to extract morphological traits of plant organs from 3D point clouds as a database for an architectural plant model," *Ecological Model.*, vol. 200, no. 1/2, pp. 119–129, 2007.

[59] F. E. Nicodemus, J. C. Richmond, J. J. Hsia, I. W. Ginsberg, and T. Limperis, *Geometrical Considerations and Nomenclature for Reflectance*. Washington, DC, USA: National Bureau of Standards, U.S. Government Printing Office, 1977.

[60] J. Xiong, G. Toller, S. J. Qiang, B. Wenny, A. Angal, and W. Barnes, MODIS Level 1B Algorithm Theoretical Basis Document (ATBD-MOD-02). NASA Goddard Space Flight Cent: MODIS Characterization Support Team, 2005.

[61] D. S. Kimes and P. J. Sellers, "Inferring hemispherical reflectance of the earth's surface for global energy budgets from remotely sensed nadir or directional radiance values," *Remote Sens. Environ.*, vol. 18, no. 3, pp. 205–223, 1985.

[62] Y. Livny, F. L. Yan, M. Olson, B. Q. Chen, H. Zhang, and J. El-Sana, "Automatic reconstruction of tree skeletal structures from point clouds," in *Proc. ACM SIGGRAPH Asia 2010 Papers*, 2010, Art. no. 151.

[63] S. Paulus, J. Behmann, A.-K. Mahlein, L. Plümer, and H. Kuhlmann, "Low-cost 3D systems: Suitable tools for plant phenotyping," *Sensors (Basel)*, vol. 14, no. 2, pp. 3001–3018, Feb. 2014.

Zhu Tao received the B.S. degree in marine technology from Shanghai Ocean University, Shanghai, China, in 2015. He is currently working toward the Ph.D. degree in cartography and geographic information system at East China Normal University, Shanghai, China.

His research interests include the quantitative remote sensing of vegetation and 3-D RT modeling.

From 2019 to 2020, Tao was the recipient of the scholarship under the State Scholarship Fund to pursue study in the DART team of CESBIO at Paul Sabatier University, France as a Visiting Ph.D. Student.

Runhe Shi was born in Shanghai, China, in 1979. He received the B.S. degree in geography from East China Normal University, Shanghai, China, in 2001, and the Ph.D. degree in geographic information systems from the Institute of Geographic Sciences and Natural Resources Research, Chinese Academy of Sciences, Guangzhou, China, in 2006.

From 2006 to 2009, he was a Lecturer with the Key Laboratory of Geographic Information Science (KLGIS), Ministry of Education, China. Since 2009, he has been an Associate Professor with the School of Geographic Sciences, East China Normal University and the KLGIS. He has authored more than 100 articles and conference papers, and holds four patents. His research interests include quantitative remote sensing of vegetation, remote sensing applications interrestrial ecosystems for sustainability, and applying remote sensing and GIS in the investigation of current environmental issues.

Dr. Shi was a recipient of the Excellent Paper Award for Youth Scientist by China Society of Natural Resources in 2006, and named as a Chenguang Scholar by Shanghai Education Development Foundation in 2008.

Jean-Philippe Gastellu-Etchegorry received the Ph.D. degree in solar physics from Paul Sabatier University (PSU), Toulouse, France, in 1983, and the Ph.D. degree in remote sensing and digital image processing from PSU, in 1989.

In 1990, after five years in Gadjah Mada University Remote Sensing Center (Indonesia) and Bangkok (Thailand), he was an Associate Professor with PSU and led the IRAP Remote Sensing team. In 1995, he joined CESBIO where he led the modeling team for 15 years. In 1997, he was a Full Professor with PSU. For 17 years, he headed the AUF Remote Sensing Society (3000 members). Since 2007, he has been a CESBIO Deputy Director and President of the Scientific Council of IUT, a Major Faculty with PSU. Since 1992, he heads the team that develops the DART model that simulates fluorescence, radiative budget and satellite/airborne/*in-situ* spectroradiometer and LIDAR acquisitions of natural and urban landscapes. DART was patented in 2003. PSU gave 460 licenses to research and space centers (NASA, KCL, CAS, etc.). He wrote 168 papers (rate A), three books, and book chapters. His research interests include radiative transfer modeling and applications.

Prof. Gastellu-Etchegorry is a cochair of MIRS TC (IEEE GRSS) and Executive Editor of the *Journal of Remote Sensing*.

Jiayin Shi was born in Shanghai, China, in 1996. She is currently working toward the master's degree in cartography and geography information system at East China Normal University, Shanghai, China.

Since 2019, she has been a member of Joint Laboratory of Environmental Remote Sensing and Data Assimilation and Key Laboratory of Geographic Information Science, Ministry of Education, East China Normal University. Her research interests include remote sensing of vegetation and hyperspectral.

Ms. Shi was the recipient of the second prize of the 17th Huawei Cup Mathematical Modeling Competition for Postgraduates.

Bo Tian received the B.S. degree in forest remote sensing from Southwest Forestry University, China, in 1999, and the Ph.D. degree in physical geography from State Key Laboratory of Estuary and Coastal Research, East China Normal University, China, in 2008.

From 1999 to 2004, he was staff in Northwest Institute of Forest Inventory, Planning, and Design, State Forestry Administration, China. Since 2016, he has been an Associate Professor with SKLEC, East China Normal University. He has conducted more than 10 national-level research projects and authored more than 50 academic papers. His research interests include coastal wetlands of remote sensing, global coastal change, and sustainable management, and cloud computing in remote sensing. He is also an active member of the Society of Wetland Scientists.

Nan Wu received the B.S. degree in forestry (major) and landscape (minor) from Anhui Agriculture University, Anhui, China, in 2015, and the M.S. degree in forestry management from Chinese Academy of Forestry, Beijing, China, in 2018. She is currently working toward the Ph.D. degree in cartography and geographic information system at East China Normal University, Shanghai, China.

Her research interests include the vegetation remote sensing, classification, and biomass inversion.

Wei Gao received the B.S. degree in applied meteorology from Nanjing Institute of Meteorology, Nanjing, China, in 1982, the M.S. degree in agro-micrometeorology and modeling from Mississippi State University, Starkville, MS, USA, in 1992, and the Ph.D. degree in applied meteorology from Purdue University, West Lafayette, IN, USA, in 1997.

He is a Professor with the Department of Ecosystem Science and Sustainability, Warner College of Natural Resources, Colorado State University, Fort Collins, CO, USA. He has authored/coauthored more than 200 academic papers and edited 21 books, scientific proceedings, and journal special issues. His research interests include atmospheric/UV radiation and modeling, remote sensing application in ecosystems, regional climate/ecosystems modeling, and the impact of climate change on agriculture/ecosystems.

Prof. Gao is a fellow of the SPIE—International Society for Optics and Photonics.